Journal Pre-proof

Space-Angle Discontinuous Galerkin Method for Radiative Transfer between Concentric Cylinders

Hang Wang, Reza Abedi, Saba Mudaliar

PII: S0022-4073(20)30362-9
DOI: https://doi.org/10.1016/j.jqsrt.2020.107281
Reference: JQSRT 107281

To appear in: *Journal of Quantitative Spectroscopy & Radiative Transfer*

Received date: 4 May 2020
Revised date: 24 August 2020
Accepted date: 24 August 2020

Please cite this article as: Hang Wang, Reza Abedi, Saba Mudaliar, Space-Angle Discontinuous Galerkin Method for Radiative Transfer between Concentric Cylinders, *Journal of Quantitative Spectroscopy & Radiative Transfer* (2020), doi: https://doi.org/10.1016/j.jqsrt.2020.107281

Highlights

- Discontinuous Galerkin Method (DGM) for solving radiative transfer equation (RTE)
- DGM employed in both space and angles is superior to hybrid methods
- Convergence in polynomial order and mesh refinement is established
- Comparison with benchmark results shows good agreement
- Numerical examples show how DGM captures discontinuous solutions.

Space-Angle Discontinuous Galerkin Method for Radiative Transfer between Concentric Cylinders

Hang Wang, Reza Abedi, Saba Mudaliar

Abstract

The integro-differential radiative transfer equation (RTE) for concentric cylinders problem involving scattering, absorption and emission is solved using the discontinuous Galerkin (DG) finite element method (FEM). The space-angle DG method directly solves the cylindrically-symmetric RTE as a three-dimensional problem, where a 1D spatially domain in radial distance r is twice extruded in the cosine of polar angle (μ) and the difference in azimuthal angle ($\tilde{\varphi}$) directions. Thus, the method has a higher accuracy than hybrid FEM-Discrete Ordinate (S_N) and FEM-Spherical Harmonic (P_N) methods. This is reflected by numerically verified convergence rate of $p+1$ for smooth problems and space-angle polynomial interpolation order of p. The axisymmetric RTE formulation is more complicated than the plane-parallel formulation, for having two independent angle directions (μ and $\tilde{\varphi}$) and an extra derivative term with respect to $\tilde{\varphi}$ in the differential equation. This results in a complex characteristic structure in $r-\tilde{\varphi}$ plane with strong discontinuity lines in radiation intensity I. A method of characteristics is formulated and implemented to verify the DG formulation and demonstrate its accuracy when such strong discontinuities persist in the solution, specifically when there are no scattering and absorption terms. The relaxation of inter-element continuity constraint of continuous FEMs by this DG method implies its superiority in numerically capturing such discontinuities. Finally, a benchmark problem pertained to heat radiation in a gray gas and another one with nonzero phase function demonstrate the effectiveness of the method in modeling black-body and scattering angular integration terms.

Keywords: Radiate transfer equation, discontinuous Galerkin, space-angle, method of characteristics, concentric cylinders, phase function, convergence rate.

1 Introduction

The *Radiative Transfer Equation* (RTE), a first order integro-differential equation, describes the radiation intensity while propagating in an absorbing and scattering medium. The RTE plays an important role in radiation transfer in atmosphere, semitransparent liquid and solids, porous materials, and many other participating media [1, 2]. Different numerical methods have been formulated to solve the RTE over the past few decades. These methods, including *Finite Volume* (FV) method [3] and *Finite Element Method* (FEM) [4], are commonly hybridized with the *Discrete Ordinates Method* (S_N or DOM) [5, 6] or *Spherical Harmonic Method* (P_N) [7, 8, 9] to handle the integrals over the solid angle.

In S_N methods, the angular dependence of radiation intensity in the RTE is decoupled by the angular discretization using a discrete set of directions (discrete ordinates) while the integral terms are replaced by quadratures. The spatial dependence in the RTE is discretized by the numerical methods mentioned above. Thus, the RTE and its corresponding boundary conditions are transformed into a set of *Partial Differential Equations* (PDEs) only in terms of the spatial coordinates. Two drawbacks of the classical S_N method are known as *false scattering* and the *ray-effect* [10] that mainly caused by the form of angular discretization [11]. In addition,

the S_N method can be problematic when specularly reflecting boundaries are present [12]. If a reflected beam on the boundary does not coincide with any discrete ordinate, the intensity of the specularly reflected beam is generally undetermined. Besides, special schemes are needed in the DOM for coping with the angular derivative terms in the RTE in curvilinear coordinates [13]; that is, the angular redistribution [14] makes it difficult to handle the angular derivative terms in the RTE.

In P_N methods, the radiation intensity field is approximated by an orthogonal series of spherical harmonics, thereby giving the method its name [1]. In the spherical harmonics series, each term has one spatial coefficient and one angular coefficient. After the integration, the expansion coefficients are formulated into a set of PDEs. The drawbacks of the P_N method are the derivation of the set of PDEs and the corresponding boundary conditions for high-order approximations, tendency of getting nonphysical oscillations and negative values for radiation intensity for high order approximations [15], and the lack of accuracy in optically thin media [16].

The (continuous) FEM is a versatile method that can simulate a wide range of problems in scientific and engineering fields which allows complex geometries. It has also been used for solving the RTE in the spatial domain by Shmygevskii [17], Krim [18], Razzaghi [19], Sallah [20], and Egger *et al.* [21]. When solving the RTE in spatial domain by the FEM, the radiation intensity is approximated by a series of shape functions in space. FEMs are generally preferred over FV and *Finite Difference* (FD) methods if higher orders of accuracy are sought. However, continuous FEMs do have a disadvantage in dealing with discontinuous and high gradient solution features. This is particularly important for the RTE, since the propagation of rays along characteristics can result is strong discontinuities in radiation intensity. The *Discontinuous Galerkin* (DG) method is more appropriate for this class of problems, including the RTE, since it relaxes the strong inter-element continuity of continuous FEMs.

The DG method was originally introduced by Reed and Hill [22] to study the neutron transport equation. For DG methods the basis functions are discontinuous across element interfaces; accordingly the jump between interior traces of solution and the so-called numerical fluxes is weakly enforced on inter-element boundaries. DG methods are specifically suitable for hyperbolic PDEs and the RTE, since the evolution of solution along characteristics can result in (strong) discontinuities. Several hybrid DG methods such as the S_N-DG method [23, 24, 25, 26, 27, 28], and the P_N-DG method [29] have been proposed, wherein the spatial domain is discretized by the DG method.

One can take advantage of FEM and DG methods to discretize the entire spatial and angular domain rather than only the spatial domain, as in the aforementioned hybrid DG methods. Liu [30] and Pontaza [31] used the FEM in both space and angle to solve the one-dimensional RTE. Castro and Trelles [32] developed the spatial and angular finite element to solve multi-dimensional RTE with high order of accuracy. Gao and Zhao [33, 34] associated the DG in space with a piece-wise constant FEM in angle. As in the spatial domain, continuous methods may fail to accurately capture discontinuities of the solution that can occur in the angular domain. Formulating a DG method in both space and angle is desirable since it prevents the artificial continuity constraint of hybrid DG methods in angle. Moreover, arbitrarily high orders of accuracy can be achieved both in space and angle directions. Kophazi and Lathouwers [35] implemented the DG method in both space and angle to solve the Boltzmann transport equation. Kitzmann *et al.* [36] solved the one-dimensional RTE with spherical symmetry by the DG method. In previous works [37, 38], a high order space-angle discontinuous Galerkin (DG) method for the plane-parallel RTE was proposed.

There are many fewer computational works for the steady state radiative heat transfer in one-dimensional cylindrical medium compared to plane-parallel and some other RTEs. Some numerical methods formulated for this problem are *Monte Carlo* (MC) [39] and variational [40, 41, 42] methods. Nowadays, with the significant improvements to computing power, the

MC method can solve radiative transfer problems efficiently and accurately. In fact, due to its accuracy, the MC method has been used to solve several benchmark problems to evaluate the performance of other methods [43, 44]. Besides, the MC method can easily handle complex geometries and have a low algorithmic complexity. However, it has some disadvantages. For example, it becomes very slow because of the exponentially increasing number of photon interactions when intensive scattering problems are considered. For the computation of conduction and/or convection parts, it is difficult for the MC method to match the required grid size needed to couple with grid-based methods, whereas, forming such couplings is relatively easy for the DG method proposed here. Regardless of the choice of numerical method, a few difficulties associated with the one-dimensional cylindrical RTE are: (1) it involves two independent variables in angle direction, which results in a high dimensional problem in spatial and angular domain; (2) an additional angular derivative term in the RTE in curvilinear coordinates requires the specification of target fluxes and their integration on new angle-normal element interfaces; (3) the additional angular term results in curved characteristics in space and angle and more complex jump manifolds for radiation intensity. For simplification, only the steady state radiative transfer in gray media is considered and the spectral radiation is not discussed in this paper. However, the existing approaches to band correlation can help study the spectral properties by providing the radiative intensity in a set of gray gases and the probability density function (PDF) of absorption coefficient [45], *e.g.,* k-distribution method [46], correlated-k method [47, 48] and spectral-line-weighted sum-of-gray-gases (SLWSGG) [49, 50].

The remainder of manuscript is structured as follows. The formulations of the method of characteristic and the DG method for the steady state RTE in one-dimensional cylindrical coordinates are presented in §2. The implementation of the DG method and the required extrusion operations in the angle direction and the implementation of the method of characteristics are described in §3. Next, several numerical examples are presented in §4 to verify and validate the DG formulation. This includes the use of *Method of Manufactured Solution* (MMS), an example of a sharp discontinuous solution in space and angle obtained by the method of characteristic, a benchmark problem from [40], and another problem in an anisotropic scattering medium. Final conclusions are drawn in §5.

2 Mathematical description

2.1 Radiation transfer equation and boundary conditions

The general form of RTE for a gray medium is,

$$\frac{\mathrm{d}I(\boldsymbol{x},\hat{\boldsymbol{s}})}{\mathrm{d}s} = -\beta I(\boldsymbol{x},\hat{\boldsymbol{s}}) + \kappa I_b(\boldsymbol{x}) + \frac{\sigma_s}{4\pi}\oint_{4\pi} I(\boldsymbol{x},\hat{\boldsymbol{s}}')\Phi(\hat{\boldsymbol{s}},\hat{\boldsymbol{s}}')\mathrm{d}s' + S(\boldsymbol{x},\hat{\boldsymbol{s}}). \tag{1}$$

This equation describes the change of radiation intensity $I(\boldsymbol{x},\hat{\boldsymbol{s}})$ at spatial location $\boldsymbol{x}$ along the path $\mathrm{d}s$ in the angle space with angle coordinate $\hat{\boldsymbol{s}}$. The values β, κ, and σ_s, are the spatial-dependent extinction, absorption, and scattering coefficients, respectively. The anisotropic scattering phase function is represented by $\Phi(\hat{\boldsymbol{s}},\hat{\boldsymbol{s}}')$ and $\boldsymbol{s}'$ is the solid angle for phase function integration. The solid angle differential for $\boldsymbol{s}'$ is denoted by $\mathrm{d}s'$. The spatial-dependent total black-body radiation intensity is given by I_b. The source term is denoted by $S(\boldsymbol{x},\hat{\boldsymbol{s}})$. If radiative equilibrium prevails, I_b is [2],

$$I_b(\boldsymbol{x}) = \frac{1}{4\pi}\oint_{4\pi} I(\boldsymbol{x},\hat{\boldsymbol{s}}')\mathrm{d}s'. \tag{2}$$

For one-dimensional axisymmetric problems (infinite in z direction), the RTE for a gray medium that emits, absorbs and anisotropically scatters in an cylindrical enclosure is written as,

$$\sin\theta\cos\tilde{\varphi}\frac{\partial I(r,\mu,\tilde{\varphi})}{\partial r} - \frac{\sin\theta\sin\tilde{\varphi}}{r}\frac{\partial I(r,\mu,\tilde{\varphi})}{\partial\tilde{\varphi}}$$
$$= -\beta I(r,\mu,\tilde{\varphi}) + \kappa I_b(r) + \frac{\sigma_s}{4\pi}\int_{-\pi}^{\pi}\int_{-1}^{1} I(r,\mu',\tilde{\varphi}')\Phi(\mu,\tilde{\varphi},\mu',\tilde{\varphi}')\mathrm{d}\mu'\mathrm{d}\tilde{\varphi}' + S(r,\mu,\tilde{\varphi}), \tag{3}$$

where the spatial location $\boldsymbol{x}$ is represented in polar coordinates with r, φ_x, and z corresponding to radial distance, spatial azimuthal angle, and coordinate along the axis of symmetry, respectively. The spherical coordinates of solid angle $\hat{\boldsymbol{s}}$ are polar angle θ and angular azimuthal angle φ_s, as shown in fig. 1. The radiation intensity is expressed as $I(r,\mu,\tilde{\varphi})$, where $\mu = \cos(\theta)$ [1] and $\tilde{\varphi}$ is the azimuthal angle measured from the local radial direction; that is, $\tilde{\varphi} = \varphi_s - \varphi_x$. The spatial coordinates z and φ_x are removed due to invariance along the axis of symmetry, and angular symmetry of the problem (enabling the use of $\tilde{\varphi}$ instead of two coordinates φ_s and φ_x). The direction of the ray at point $\boldsymbol{x}$ and angular coordinates θ and $\tilde{\varphi}$ is expressed as $\hat{\boldsymbol{s}} = (\sin\theta\cos\tilde{\varphi}, \sin\theta\sin\tilde{\varphi})$. To guarantee the energy conservation, the phase function is normalized as,

$$\frac{1}{4\pi}\int_{-\pi}^{\pi}\int_{-1}^{1}\Phi(\mu,\tilde{\varphi},\mu',\tilde{\varphi}')\mathrm{d}\mu'\mathrm{d}\tilde{\varphi}' = 1. \tag{4}$$

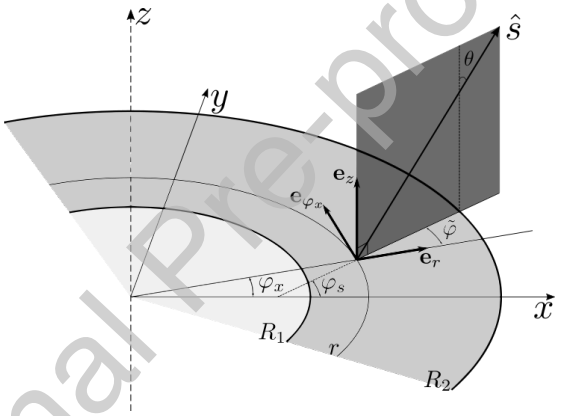

Figure 1: Cylindrical coordinates for the one-dimensional RTE.

Equation (3) is solved on the three-dimensional domain $(r,\mu,\tilde{\varphi}) \in \Omega = (R_1, R_2)\times(-1,1)\times(-\pi,\pi)$, where R_1 and R_2 are the radii of inner and outer surface walls; *cf.* Figure 1. For an opaque surface that emits and reflects specularly and diffusively, the radiation intensity on the domain boundary, R_w, with index $w \in \{1,2\}$ referring to the inner and outer radii, is given by [2],

$$I(R_w,\hat{\boldsymbol{s}}) = \epsilon(R_w)I_b(R_w) + \frac{\rho^d(R_w)}{\pi}\int_{\hat{\boldsymbol{s}}'\cdot\boldsymbol{n}>0} I(R_w,\hat{\boldsymbol{s}}')\hat{\boldsymbol{s}}'\cdot\boldsymbol{n}\mathrm{d}\mu'\mathrm{d}\tilde{\varphi}' + \rho^s(R_w)I(R_w,\hat{\boldsymbol{s}}_s), \tag{5}$$

where $\boldsymbol{n}$ is the surface normal, ϵ is the wall emissivity and ρ is the reflectivity divided in a diffuse component ρ_d and a specular component ρ_s with the relationship, $\rho = \rho_d + \rho_s$. Since the surface is opaque, $\epsilon + \rho = 1$. The first term on the right side of (5) arises from the surface emission. Under the assumption of diffuse-gray $I_b = n^2\sigma T^4/\pi$ [2]. The second term is the diffusively reflected component. The third term is the specularly reflected component, where $\hat{\boldsymbol{s}}_s$ is the specular direction defined as the direction of a light beam traveling from the surface in a direction of $\hat{\boldsymbol{s}}$ after a specular reflection. This direction is given by $\hat{\boldsymbol{s}}_s = \hat{\boldsymbol{s}} - 2(\hat{\boldsymbol{s}}\cdot\boldsymbol{n})\boldsymbol{n}$. Equation (5) is specified on the inflow boundaries which are defined when $\hat{\boldsymbol{s}}\cdot\boldsymbol{n} > 0$.

[1] Since, the spatial coordinate (r,φ_x,z) does not include a spatial azimuthal angle, the subscript s is dropped from angular azimuthal angle and its cosine value for brevity.

2.2 Characteristic directions for the RTE

The method of characteristics was firstly introduced to solve the RTE in 1970 [51]. Rukolaine *et al.* [12] extended this method to solve the 2-D RTE in cylindrical coordinates with complex boundary conditions. By solving *Ordinary Differential Equations* (ODEs) along the characteristic lines, this method provides physical insight on how the rays propagate in the space-angle domain and can be computationally advantageous for high spatial or angular dimension problems.

To validate DG solution, the method of characteristics is introduced. Along a characteristic line, the RTE takes the form,

$$\frac{\mathrm{d}I}{\mathrm{d}s} = \breve{S}(r,\mu,\tilde{\varphi}), \tag{6}$$

where $\breve{S}$ is the *total source term* which is the right hand side of (3),

$$\breve{S}(r,\mu,\tilde{\varphi}) = -\beta I(r,\mu,\tilde{\varphi}) + \kappa I_b(r) + \frac{\sigma_s}{4\pi}\int_{-\pi}^{\pi}\int_{-1}^{1} I(r,\mu',\tilde{\varphi}')\Phi(\mu,\tilde{\varphi},\mu',\tilde{\varphi}')\mathrm{d}\mu'\mathrm{d}\tilde{\varphi}' + S(r,\mu,\tilde{\varphi}). \tag{7}$$

Equation (6) is written as,

$$\boldsymbol{V}\cdot\left(\frac{\partial I}{\partial r},\frac{\partial I}{\partial \mu},\frac{\partial I}{\partial \tilde{\varphi}}\right) = |\boldsymbol{V}|\frac{\mathrm{d}I}{\mathrm{d}l} = \breve{S}, \tag{8}$$

where $\boldsymbol{V} = \left(\sin\theta\cos\tilde{\varphi}, 0, -\frac{\sin\theta\sin\tilde{\varphi}}{r}\right)$, $\tilde{\boldsymbol{e}} = \frac{\boldsymbol{V}}{|\boldsymbol{V}|}$ is the unit vector (direction) along the characteristic, and l is the length coordinate along the characteristic starting from the inflow (upstream) towards the outflow (downstream), tangent to $\tilde{\boldsymbol{e}}$ as shown in fig. 2. The relation between the increments of space-angle coordinates and characteristic length is,

$$\begin{aligned} \mathrm{d}r &= \frac{\sin\theta\cos\tilde{\varphi}}{|\boldsymbol{V}|}\mathrm{d}l, \\ \mathrm{d}\mu &= 0, \\ \mathrm{d}\tilde{\varphi} &= -\frac{\sin\theta\sin\tilde{\varphi}}{r|\boldsymbol{V}|}\mathrm{d}l, \end{aligned} \tag{9}$$

accordingly, characteristic lines stay in the $r-\tilde{\varphi}$ plane, since $\mathrm{d}\mu = 0$.

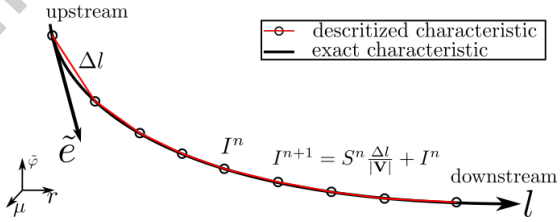

Figure 2: Coordinate along a characteristic line.

The ODE (8) is solved starting from inflow parts of spatial boundary of Ω (at R_1 or R_2), where I is given at the beginning of characteristic lines as initial condition. This can easily be done when there are no angular integration terms in (7), that is when I_b, $\Phi = 0$. For details of the implementation of this method when these angle integrals are present, refer to §3.2.

2.3 Discontinuous Galerkin formulation

Figure 3 shows an $m\times n\times l$ tensor product discretization of space-angle domain $\Omega = (R_1,R_2)\times(-1,1)\times(-\pi,\pi)$, discretized into $\{r_0,r_1,...,r_m\}$, $\{\mu_0,\mu_1,...,\mu_n\}$, and $\{\tilde{\varphi}_0,\tilde{\varphi}_1,...,\tilde{\varphi}_l\}$ along r, μ,

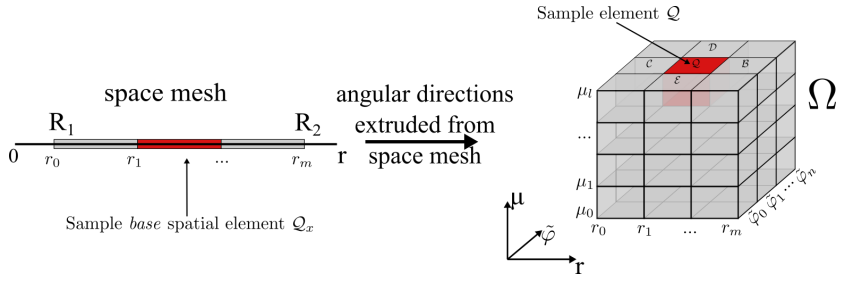

Figure 3: The illustration of the extrusion of the spatial domain in angle directions μ and $\tilde{\varphi}$. The left figure shows the one-dimensional spatial elements and the right shows their extrusion to form the three-dimensional domain Ω.

and $\tilde{\varphi}$ directions, respectively, for $r_0 = R_1$, $r_m = R_2$, $\mu_0 = -1$, $\mu_n = 1$, $\tilde{\varphi}_0 = -\pi$, and $\tilde{\varphi}_l = \pi$. For an arbitrary element $\mathcal{Q} \in \Omega$ in fig. 3, the interior residual corresponding to PDE (3) is,

$$\begin{aligned}\mathcal{R}_{\mathcal{Q}} = \sin\theta\cos\tilde{\varphi}\frac{\partial I}{\partial r} - \frac{\sin\theta\sin\tilde{\varphi}}{r}\frac{\partial I}{\partial\tilde{\varphi}} + \beta I - \kappa I_b \\ -\frac{\sigma_s}{4\pi}\int_{-\pi}^{\pi}\int_{-1}^{1} I(r,\mu',\tilde{\varphi}')\Phi(\mu,\tilde{\varphi},\mu',\tilde{\varphi}')\mathrm{d}\mu'\mathrm{d}\tilde{\varphi}' - S(r,\mu,\tilde{\varphi}).\end{aligned} \tag{10}$$

For DG methods the continuity of solution on the boundary of elements is weakly satisfied relative to a *target* or *numerical flux* I^*. As mentioned in §1, this relaxes the continuity constraint of continuous finite element methods, which can be both nonphysical and not accurately model the propagation of waves along characteristic lines. For RTE, the residual on $\partial\mathcal{Q}$, the boundaries of the element $\mathcal{Q}$, corresponds to differential operator $\mathrm{d}I(\boldsymbol{x},\hat{\boldsymbol{s}})\,/\,\mathrm{d}s$ in (1) and is expressed as,

$$\mathcal{R}_{\partial\mathcal{Q}} = \hat{\boldsymbol{s}}\cdot\boldsymbol{n}(I^* - I), \tag{11}$$

where $\boldsymbol{n} = (n_r, n_{\varphi_x}, n_z)$ is the normal direction on $\partial\mathcal{Q}$ in spatial coordinates and $\hat{\boldsymbol{s}}$ is the direction of radiation.

The target value I^* corresponds to the upstream value along the direction of wave propagation and is given by,

$$I^* = \begin{cases} I & \hat{\boldsymbol{s}}\cdot\boldsymbol{n} \geq 0 \text{ outflow boundary} \\ I^{out} & \hat{\boldsymbol{s}}\cdot\boldsymbol{n} < 0 \text{ inflow boundary} \end{cases} \quad \Rightarrow \quad \mathcal{R}_{\partial\mathcal{Q}} = \begin{cases} 0 & \hat{\boldsymbol{s}}\cdot\boldsymbol{n} \geq 0 \\ \hat{\boldsymbol{s}}\cdot\boldsymbol{n}(I^{out} - I) & \hat{\boldsymbol{s}}\cdot\boldsymbol{n} < 0 \end{cases}. \tag{12}$$

That is, on outflow boundary of $\mathcal{Q}$, where $\hat{\boldsymbol{s}}\cdot\boldsymbol{n} \geq 0$, I^* is set equal to interior trace and the jump condition $\mathcal{R}_{\partial\mathcal{Q}}$ is trivially satisfied. On the other hand, the inflow boundaries correspond to $\hat{\boldsymbol{s}}\cdot\boldsymbol{n} < 0$. For inflow boundaries, the target flux is set equal to outside intensity I^{out}. When the inflow boundary of $\mathcal{Q}$ is on the boundary of domain, $\partial\Omega$, I^{out} is set to the boundary flux determined from (5). For a point on an inflow interface of $\mathcal{Q}$ that is inside Ω, I^* is set to I^{out}, the interior trace of I at the same location for the neighboring element $\mathcal{Q}^{out}$. Clearly, I^{out} is also the target value for the same point on the boundary of neighbor element $\mathcal{Q}^{out}$. For $\mathcal{Q}^{out}$ this point is on its outflow boundary and $\mathcal{R}_{\partial\mathcal{Q}}$ is trivially satisfied. That is, for any interior interface in Ω, there is exactly one non-trivially zero $\mathcal{R}_{\partial\mathcal{Q}}$ on the side that is inflow boundary. This corresponds to the downstream direction of characteristic lines; *cf.* fig. 2.

Next, the specific form of $\hat{\boldsymbol{s}}\cdot\boldsymbol{n}$ for axisymmetric RTE in (3) is discussed to determine inflow and outflow boundaries of $\mathcal{Q}$ and I^* from (12). For this configuration $\hat{\boldsymbol{s}} = (\sin\theta\sin\varphi_x, \sin\theta\sin\varphi_x, \cos\theta)$. Since the solution is invariant along z-direction and $\varphi_x = -\tilde{\varphi}$ when $\varphi_s = 0$

the expression for $\hat{\boldsymbol{s}} \cdot \boldsymbol{n}$ in (11) is simplified to,[2]

$$\hat{\boldsymbol{s}} \cdot \boldsymbol{n} = \sin\theta \cos\tilde{\varphi} n_r - \sin\theta \sin\tilde{\varphi} n_{\tilde{\varphi}}. \tag{13}$$

Note that the factors of n_r, $n_{\tilde{\varphi}}$, and n_μ (zero) in $\hat{\boldsymbol{s}} \cdot \boldsymbol{n}$ correspond to the factors of $\mathrm{d}I \,/\, \mathrm{d}r$, $\mathrm{d}I \,/\, \mathrm{d}\tilde{\varphi}$, and $\mathrm{d}I \,/\, \mathrm{d}\mu$ (zero) in (10), considering that the geometric Jacobian of the cylindrical coordinate system is equal to r.

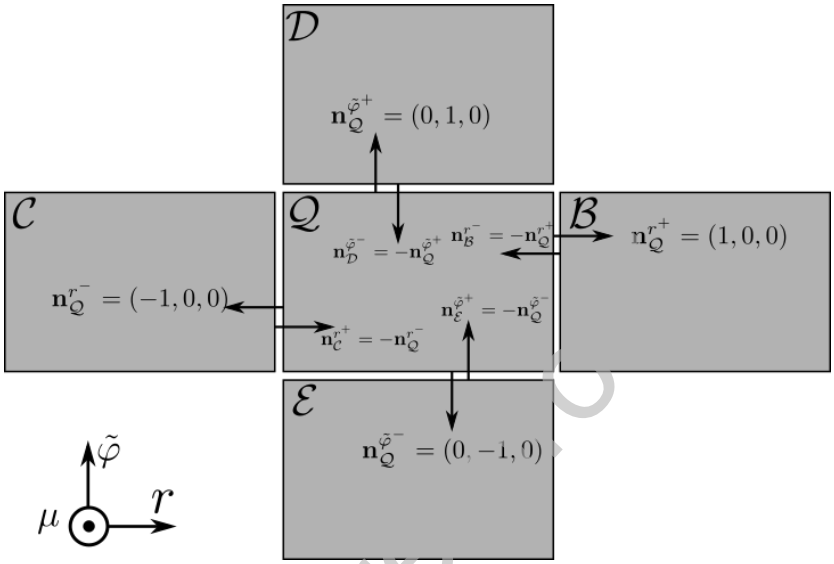

Figure 4: The illustration of normal vectors of the element $\mathcal{Q}$ and its neighboring elements on the shared boundaries in r-$\tilde{\varphi}$ plane. The subscript and superscript of normal vectors correspond to the element with normal vector and its direction, respectively.

A cubic element in fig. 3 has 6 boundaries in Ω. Figure 4 shows element $\mathcal{Q}$ and its four neighbors in the r-$\tilde{\varphi}$ plane. The two boundaries along positive and negative μ directions are not shown as $\hat{\boldsymbol{s}} \cdot \boldsymbol{n}$ is trivially zero and there is no coupling between elements in μ direction (this corresponds to the absence of $\mathrm{d}I \,/\, \mathrm{d}\mu$ term in (10)). The normal vectors for element $\mathcal{Q}$ point outward toward neighboring elements $\mathcal{B}$, $\mathcal{C}$, $\mathcal{D}$ and $\mathcal{E}$. The normals of the neighboring elements on the shared boundaries with $\mathcal{Q}$ point in the opposite directions. For normal vectors, the subscripts denote the element for which the normal vector is defined and the superscripts show the coordinate and the direction that the normal is pointing to. For example, $n_{\mathcal{Q}}^{\tilde{\varphi}^-}$ is the normal from element $\mathcal{Q}$ to $\mathcal{E}$ in the negative $\tilde{\varphi}$ direction.

The specific values of $(n_r, n_{\tilde{\varphi}}, n_\mu)$ are shown in parentheses for the four faces of the element $\mathcal{Q}$ that are in the r-$\tilde{\varphi}$ plane in fig. 4. Specifically, $(n_r, n_{\tilde{\varphi}}, n_\theta) = (\mp 1, 0, 0)$ for $\partial\mathcal{Q}_r^{\mp}$ and $(n_r, n_{\tilde{\varphi}}, n_\theta) = (0, \mp 1, 0)$ for $\partial\mathcal{Q}_{\tilde{\varphi}}^{\mp}$, respectively, and their corresponding $\hat{\boldsymbol{s}} \cdot \boldsymbol{n}$ and residuals are,

$$\hat{\boldsymbol{s}} \cdot \boldsymbol{n} = \sin\theta \cos\tilde{\varphi} n_r \quad \Rightarrow \quad \mathcal{R}_{\partial\mathcal{Q}_r} = \sin\theta \cos\tilde{\varphi} n_r (I^* - I), \quad \text{on } \partial\mathcal{Q}_r^{\mp} \tag{14a}$$

$$\hat{\boldsymbol{s}} \cdot \boldsymbol{n} = -\sin\theta \sin\tilde{\varphi} n_{\tilde{\varphi}} \quad \Rightarrow \quad \mathcal{R}_{\partial\mathcal{Q}_{\tilde{\varphi}}} = -\sin\theta \sin\tilde{\varphi} n_{\tilde{\varphi}} (I^* - I), \quad \text{on } \partial\mathcal{Q}_{\tilde{\varphi}}^{\mp} \tag{14b}$$

The coordinates $\tilde{\varphi}$ and $\mu = \cos\theta$ at each point on these four boundaries determine the value of $\hat{\boldsymbol{s}} \cdot \boldsymbol{n}$ in (14) and whether the residual is trivially zero for $\hat{\boldsymbol{s}} \cdot \boldsymbol{n} \geq 0$.

It is noted that while the boundary of Ω in fig. 3 includes r-, $\tilde{\varphi}$-, and μ-normal surfaces, boundary conditions are only enforced on r-normal spatial boundaries of the domain at $r = R_1$ and $r = R_2$, on the parts that are wave-inflow; the description of regions on $r = R_1$ and $r = R_2$

[2]Due to axisymmetry, the same expression is obtained for $\varphi_s \neq 0$.

that are inflow is provided in §3.2. For μ-normal boundaries, by default there are no boundary residuals, as for element facets at $\mu = \pm 1$ we have $n_r = n_{\tilde{\varphi}} = 0$; accordingly, the corresponding element boundary residual is zero from (13). Finally, for $\tilde{\varphi}$-normal facets, $\mathcal{R}_{\partial\mathcal{Q}_{\tilde{\varphi}}} = 0$ in (14b) as $\tilde{\varphi} = \pm\pi$ for these facets on the boundary of Ω.

In this work, the unknown intensity in each element is expressed in terms of scaled coordinates $r', \mu', \tilde{\varphi}'$,

$$r' = \frac{r - m_r}{\Delta r}$$
$$\tilde{\varphi}' = \frac{\tilde{\varphi} - m_{\tilde{\varphi}}}{\Delta\tilde{\varphi}}$$
$$\mu' = \frac{\mu - m_\mu}{\Delta\mu}$$

where m_r, $m_{\tilde{\varphi}}$, and m_μ are the minimum values of the coordinates within the element and Δr, $\Delta\tilde{\varphi}$, and $\Delta\mu$ the spans of a cubic element $\mathcal{Q}$ in r, $\tilde{\varphi}$, and μ directions, respectively. The use of scaled coordinates $(r', \tilde{\varphi}', \mu') \in [0, 1]$ prevents ill-conditioning problems that can arise if r, $\tilde{\phi}$, and μ are directly used to interpolate the solution within elements.

The discrete solution for element $\mathcal{Q}$, $I^h_{\mathcal{Q}}$, is interpolated by the tensorial product monomials of order p_r, p_μ, and $p_{\tilde{\varphi}}$, in r, μ and $\tilde{\varphi}$, respectively, and is given by,

$$I^h_{\mathcal{Q}}(r', \mu', \tilde{\varphi}') = \sum_{i=0}^{p_r}\sum_{j=0}^{p_{\tilde{\varphi}}}\sum_{k=0}^{p_\mu} a^{ijk}_{\mathcal{Q}}\, r'^i \tilde{\varphi}'^j \mu'^k, \tag{15}$$

where the coefficients $a^{ijk}_{\mathcal{Q}}$ are the unknowns for element $\mathcal{Q}$. Note that $I^h_{\mathcal{Q}}$ is zero outside the element $\mathcal{Q}$. In general, for example in the context of a p-adaptive scheme, each space-angle element $\mathcal{Q}$ can have its distinct orders $(p_r, p_{\tilde{\varphi}}, p_\mu)$. However, this option is not practiced in the numerical studies presented in §4 and a constant polynomial order $p := p_r = p_{\tilde{\varphi}} = p_\mu$ is used for all directions.

The discrete solution I^h is obtained by multiplying the interior residual (10) and boundary residual (11) by weight functions $\hat{I}$ and integrating them over the interior and boundary of elements, respectively. The discrete form of this weighted residual statement for an arbitrary element $\mathcal{Q} \in \Omega$ is,

$$\begin{aligned}\int_{\mathcal{Q}} \hat{I}_{\mathcal{Q}} \Bigg(&\sin\theta\cos\tilde{\varphi}\frac{\partial I^h_{\mathcal{Q}}}{\partial r} - \frac{\sin\theta\sin\tilde{\varphi}}{r}\frac{\partial I^h_{\mathcal{Q}}}{\partial\tilde{\varphi}} + \beta I^h_{\mathcal{Q}} - \kappa I_b - S(r, \mu, \tilde{\varphi}) \\ &- \frac{\sigma_s}{4\pi}\int_{-\pi}^{\pi}\int_{-1}^{1} I^h(r, \mu', \tilde{\varphi}')\Phi(\mu, \tilde{\varphi}, \mu', \tilde{\varphi}')\mathrm{d}\mu'\mathrm{d}\tilde{\varphi}'\Bigg) r\mathrm{d}r\mathrm{d}\mu\mathrm{d}\tilde{\varphi} \\ + \int_{\partial\mathcal{Q}_r} \hat{I}_{\mathcal{Q}} \left[\sin\theta\cos\tilde{\varphi}(I^* - I^h_{\mathcal{Q}})\right] n_r r\mathrm{d}\mu\mathrm{d}\tilde{\varphi} &+ \int_{\partial\mathcal{Q}_{\tilde{\varphi}}} \hat{I}_{\mathcal{Q}} \left[-\sin\theta\sin\tilde{\varphi}(I^* - I^h_{\mathcal{Q}})\right] n_{\tilde{\varphi}}\mathrm{d}r\mathrm{d}\mu = 0.\end{aligned} \tag{16}$$

Since a Bubnov Galerkin method is used, the weight functions, $\hat{I}_{\mathcal{Q}}$, are taken from the basis functions of the discrete solution $\hat{I}^h_{\mathcal{Q}}$, equal to monomials $r'^i\mu'^j\tilde{\varphi}'^k$ for $0 \le i \le p_r$, $0 \le j \le p_{\tilde{\varphi}}$, and $0 \le k \le p_\mu$, within the element $\mathcal{Q}$ and zero outside. The global coupling between different angle ranges $\mu \in (\mu_j, \mu_{j+1})$, $j \in \{0, \cdots, m-1\}$ and $\tilde{\varphi} \in (\tilde{\varphi}_k, \tilde{\varphi}_{k+1})$, $k \in \{0, \cdots, l-1\}$ arises from the triple phase function integral in (16) or boundary conditions, such as reflective boundary condition, that can couple all angles at $r = R_1$ and $r = R_2$; *cf.* (5).

3 Implementation

3.1 Discontinuous Galerkin implementation

The implementation of the RTE is based on a general purpose C++ software code for the solution of discontinuous Galerkin methods. This software was originally designed for the solution of

causal Spacetime Discontinuous Galerkin (cSDG) methods for elastodynamics [52], advection-diffusion equation [53], and electromagnetics [54], just to name a few. The cSDG method directly discretizes space and time with simplicial elements that satisfy a special causality constraint. The weak enforcement of the jump conditions between interior and target fluxes on the boundaries of elements provides unique opportunities to model complex interface matching problems; see for example [55, 56, 57]. However, these facet terms require more general modeling of integration cells capable of integration of coincident interior and facets cells for interface problems [58], facet and cofacet neighborhood information, and computational geometry operations.

We have used the existing functionalities of the cSDG software for the implementation of general RTEs. Specifically, the support for coupling of space with other coordinates (time in aforementioned references) simplified the implementation of space-angle coupled elements. However, a major overhaul of the software and implementation of a new geometry library (GMeshing) was required to analyze space-angle elements used for the RTE. To implement general RTEs, the software supports the extrusion of a 1D to 3D spatial domain, discretized by simplicial elements, into arbitrary number of extrusions in angle or other coordinates. For example, in fig. 3, 1D simplicial spatial elements (lines) on the left are extruded first to the 9 once-extruded simplicial elements (squares) in the $r-\tilde{\varphi}$ plane and next to twice-extruded simplicial elements (cubes) in Ω. Some specific challenges with this implementation included setting neighborhood information (facets and cofacets in spatial and extrusion directions), formation and processing of integration cells, and computational geometry information of the extruded cells. Moreover, for angle integration terms in (3) and (5) additional neighborhood information between space-angle cells and their corresponding *base* spatial elements, *e.g.,* elements $\mathcal{Q}$ and $\mathcal{Q}_x$ in fig. 3, and integration routines were required. The software architecture of GMeshing and this expanded finite element DG module are expected to be discussed in more detail in subsequent publications.

3.2 Method of characteristic

The method of characteristic is implemented in MATLAB and C++ to visualize the solution and compare the results with the DG method. The RTE formulation with or without angular integration terms (emission term and scattering term) can be modeled with this method. The forward and backward implementations of this method are discussed next.

3.2.1 Forward scheme

Characteristics corresponds to the path of radiation rays that go through the disk depicted in fig. 1. According to (9), each characteristic is invariant to μ. This implies that the characteristics remain in the $r-\tilde{\varphi}$ plane and that the characteristic lines coincide for all $r-\tilde{\varphi}$ planes at different μ values. All of the characteristics starting at the inflow boundary on the inner wall eventually reach the outflow boundary on the outer wall. However, the characteristics starting at the outer wall end at either the inner wall or the outer wall. These inflow and outflow boundaries are shown by red and blue, respectively, in fig. 5. This is because in a disk-like medium some inflow rays on the outer wall intersect the outer wall and some reach the inner wall.

To calculate the radiation intensity field, the domain is first discretized into N $r-\tilde{\varphi}$ planes for $\mu_k \in \{\mu_1, ..., \mu_N\}$. The characteristic lines and other quantities on the k^{th} $r-\tilde{\varphi}$ plane are decorated with the left superscript k, corresponding to μ_k. For example, the characteristic lines on the k^{th} plane are ${}^k l_j$ for $j \in \{1, 2, \ldots, M\}$ where M is the number of characteristic lines considered on this plane and j is the index of characteristic line. As shown in fig. 5, the characteristic lines start from points on the inflow boundaries of the domain, that is $\tilde{\varphi} \in [-\pi/2, \pi/2]$ at $r = R_1$ the inner wall and $\tilde{\varphi} \in [-\pi - \pi/2] \cup [\pi/2, \pi]$ at $r = R_2$ the outer wall. Finally, each characteristic line ${}^k l_j$ is discretized into segments separated by points ${}^k p_j^i$, with i being the index of points on this line, as shown in the figure. Thus, the radiation intensity

at the end of the segment point, ${}^{k}p_j^{i+1}$, along characteristic, ${}^{k}l_j$, is calculated by forward Euler scheme derived from (8),

$$|\boldsymbol{V}|\,\frac{{}^{k}I_j^{i+1}-{}^{k}I_j^{i}}{\Delta l}={}^{k}\breve{S}_j^{i},\qquad k\in\{1,\ldots,N\},j\in\{1,\ldots,M\},\tag{17}$$

where ${}^{k}\breve{S}_j^{i}$ is the source term at point ${}^{k}p_j^{i+1}$ and $\Delta l=\sqrt{\Delta r^2+\Delta\tilde{\varphi}^2}$ is the distance of the points ${}^{k}p_j^{i}$ and ${}^{k}p_j^{i+1}$ with relative positions Δr and $\Delta\tilde{\varphi}$ in r and $\tilde{\varphi}$ directions, respectively. This ODE starts from initial condition ${}^{k}I_j^{0}$ at the first point of characteristic ${}^{k}l_j$ on the corresponding inflow boundary; *cf.* fig. 5.

If angle coupling exists (with angular integration terms in (3)), an iterative scheme is needed to update the total source term, ${}^{k}\breve{S}_j^{i}$. The trapezoidal rule is used to approximate the integrals over the angle at ${}^{k}p_j^{i}$. Since all characteristics overlap each other over μ direction, no interpolation of solutions is needed in this direction and a trapezoidal rule is employed for angle integrations in μ direction. For example, the two points ${}^{k}p_j^{i}$ and ${}^{k-1}p_j^{i}$ are shown for the integrals in μ at p_j^{i} location in $r-\tilde{\varphi}$ planes in fig. 5. However, the solutions for solid angle integration along $\tilde{\varphi}$ need to be interpolated from existing solutions at points ${}^{k}p_j^{i}$. The trapezoidal rule based on the interpolated solutions is used for the $\tilde{\varphi}$ direction integrals. The iterations start with an initial guess, *e.g.,* the solution with no angular integration, and continues until the intensity at all points converges.

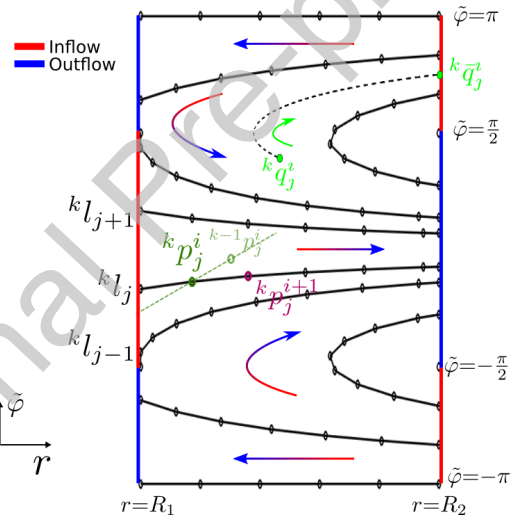

Figure 5: Schematic of the discrete set of $r-\tilde{\varphi}$ planes, characteristic lines, and points for numerical solution of the method of characteristics.

3.2.2 Backward scheme

A backward scheme is preferred if the solution is sought on a structured grid. The domain is discretized into a structured cube with points ${}^{k}q_j^{i}=(r_i,\tilde{\varphi}_j,\mu_k)$, where $r_i\in\{r_0,r_1,...,r_M\}$, $\tilde{\varphi}_j\in\{\tilde{\varphi}_0,\tilde{\varphi}_1,...,\tilde{\varphi}_L\}$, and $\mu_k\in\{\mu_0,\mu_1,...,\mu_N\}$. Since the RTE is a linear differential equation, the path of a characteristic line passing through a point, both forward and backward, is independent of the solution of radiation intensity along its path. This is reflected in the independence of the increments of the characteristic path on solution I in (9). Accordingly, the backward path of a characteristic passing through a grid point ${}^{k}q_j^{i}$, shown in green in fig. 5, can be determined by (9), without having the solution of radiation intensity along its path (shown in dashed line). Once the starting point on the inflow boundary of the domain, shown by ${}^{k}\bar{q}_j^{i}$, is determined,

the initial condition along this determined characteristic path is obtained from the boundary condition. Next, a forward Euler integration scheme similar to (17) can be used to determine the solution at ${}^k q_j^i$ from the boundary condition at ${}^k \bar{q}_j^i$. When angular integration terms in (3) are nonzero, an iterative solution scheme similar to that described in §3.2.1 is used; the initial solution (guess) corresponds to the solution with zero angle integral terms and at each iteration source term and radiation intensity are updated until the differences of radiation intensities of two successive solutions is below a user specified tolerance at all grid points.

The backward scheme has several advantages. First, the structured points ${}^k \bar{q}_j^i$ can coincide with quadrature points of a DG method discretization. This enables the computation of the error between discrete DG solution and a solution represented by this backward method of characteristics. The latter solution can be considered as the (exact) reference solution as long as sufficiently small Δl is chosen for the integration of solution in (17). Second, since a structured grid is used in all directions, the points in $\tilde{\varphi}$ direction also coincide; thus, unlike the forward scheme in §3.2.1 there is no need to interpolate the solution in $\tilde{\varphi}$ direction when angular integration terms are nonzero. Third, as will be discussed in §4.2, *cf.* fig. 8, the characteristic lines are sparse in certain parts of the domain. Using a backward scheme ensures that the solution can be represented by uniform resolutions in all directions. However, it is noted that the backward scheme is more expensive as for each point, the solution along one characteristic is required. In contrast, in forward scheme, the solution along each characteristic line represents many solution points.

4 Numerical examples

In this section, the DG method is first verified for problems with exact smooth solutions; the MMS is used in §4.1 to first capture polynomial solutions that belong to discrete solution space and next obtain the convergence rate of the DG method. A furnace radiation problem for which closed form analytical solution does not exist is studied in §4.2. The method of characteristics is used to verify the DG method for this problem and demonstrate the form of characteristics for this axisymmetric RTE formulation. Finally, a blackbody emission problem and an anisotropic scattering problem are presented in §4.3.

4.1 Method of manufactured solution

The MMS is used to validate formulation and implementation of the DG RTE method. In the MMS, a function I^{M} is chosen to satisfy the RTE,

$$I(r, \mu, \tilde{\varphi}) = I^{\mathrm{M}}(r, \mu, \tilde{\varphi}). \tag{18}$$

The source term in (3) is determined such that I^{M} satisfies this equation. Accordingly, source term, specifically denoted by S^{M} for the MMS, is obtained by plugging (18) in the RTE to obtain,

$$\begin{aligned} S^{\mathrm{M}} = {} & \sin\theta\cos\tilde{\varphi}\frac{\partial I^{\mathrm{M}}}{\partial r} - \frac{\sin\theta\sin\tilde{\varphi}}{r}\frac{\partial I^{\mathrm{M}}}{\partial \tilde{\varphi}} + \beta I^{\mathrm{M}} - \kappa I_b \\ & - \frac{\sigma_s}{4\pi}\int_{-\pi}^{\pi}\int_{-1}^{1} I^{\mathrm{M}}(r, \mu', \tilde{\varphi}')\Phi(\mu, \tilde{\varphi}, \mu', \tilde{\varphi}')\mathrm{d}\mu'\mathrm{d}\tilde{\varphi}'. \end{aligned} \tag{19}$$

Conversely, if the RTE problem is solved with the source term (19) and boundary conditions consistent with I^{M} on the inflow parts of the spatial boundary of domain at R_1 and R_2, the function I^{M} is recovered as the exact solution of the RTE (3). In discrete setting, if the manufactured solution I^{M} belongs to the space of finite element solution, *i.e.,* when it is a polynomial of order equal or less than that used to interpolate I^h in (15), the exact solution

I^{M} is recovered. Otherwise, I^h asymptotically converges to I^{M} as finer meshes (h-refinement) or higher order polynomials for I^h (p-enrichment) are used. The former and latter cases are applied for problems in §4.1.1 and §4.1.2, respectively.

4.1.1 Validation study for polynomial exact solutions

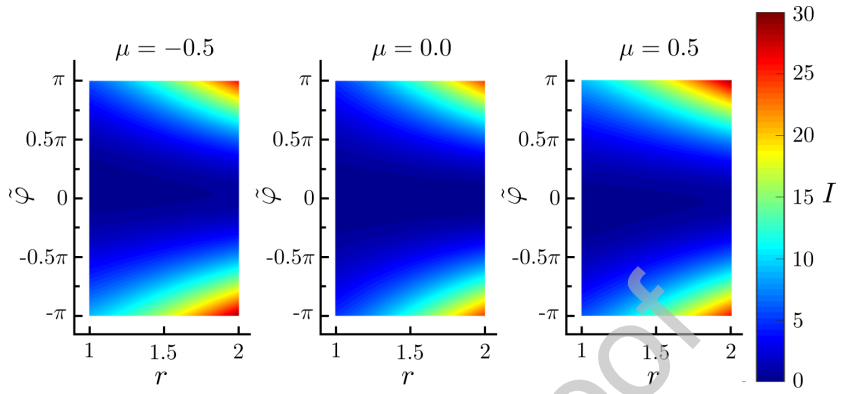

Figure 6: Validation of the DG RTE method by the MMS for second order polynomial in space and angle for I^{M}. The contour plots in $r-\tilde{\varphi}$ plane are sliced in μ direction at $\mu = -0.5,\ 0,\ 0.5$.

Two cases are conducted for validating the formulation and implementation in an annulus with inner and outer radii of $R_1 = 1$ and $R_2 = 2$, respectively. In the first case, the MS solution I^{M} is given as a second order polynomial in both space and angle,

$$I^{\mathrm{M}}(r,\mu,\tilde{\varphi}) = r^2\mu^2 + r^2\tilde{\varphi}^2 - r\mu^2 - r\tilde{\varphi}^2 + \mu^2\tilde{\varphi}^2 + \mu\tilde{\varphi} + \frac{1}{2}\tilde{\varphi}^2. \tag{20}$$

The phase function Φ and black-body radiation I_b are equal to zero. The DG method recovers the exact solution to to within machine precision. Several contour plots of the solution in $r-\tilde{\varphi}$ planes are shown in fig. 6. In the second case, the MS solution I^{M} remains the same as in the first case in (20). The black-body radiation $I_b = (1/4\pi)\oint_{4\pi} I\mathrm{d}s'$ is assumed at radiative equilibrium; *cf.* (2). The phase function is set to $\Phi = 1$ for an isotropic scattering. Again, the DG method recovers the exact solution to within machine precision.

4.1.2 Convergence study

The following harmonic function is used as the manufactured solution to perform a convergence study for the proposed DG method,

$$I^{\mathrm{M}}(r,\mu,\tilde{\varphi}) = \sin(\pi r)\sin(\pi\mu)\sin(\pi\tilde{\varphi}). \tag{21}$$

The L2 norm of the point-wise error ε between the discrete and manufactured solution is used to characterize the numerical error,

$$\text{Point-wise error :} \qquad \varepsilon(r,\mu,\tilde{\varphi}) = I^h(r,\mu,\tilde{\varphi}) - I^{\mathrm{M}}(r,\mu,\tilde{\varphi}), \tag{22a}$$

$$\text{L2 norm of error :} \qquad L_2(\varepsilon) = \sqrt{\int_\Omega |\varepsilon|^2 \mathrm{d}\Omega}. \tag{22b}$$

Since polynomials are used for the discrete solution in (15), I^h cannot exactly represent the manufactured solution (21) and the numerical error is nonezero for all element sizes and polynomial orders. The spatial domain corresponds to an annulus with inner and outer radii

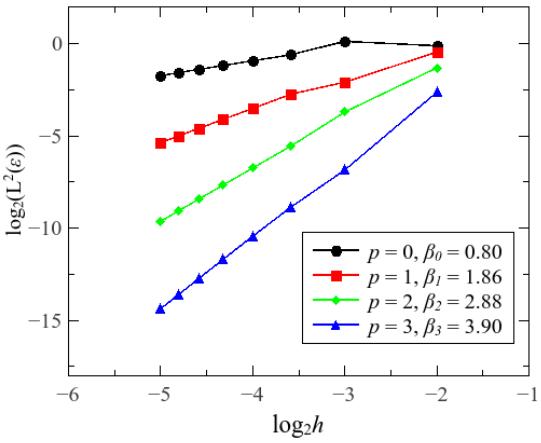

Figure 7: Convergence study of the DG RTE solution for the harmonic manufactured solution. The asymptotic convergence rate $\beta_p = p + 1$ is achieved as $h \to 0$ for $p = 0$ to $p = 3$.

of $R_1 = 1$ and $R_2 = 2$, respectively. The coarsest mesh used for convergence study contains four elements in space, corresponding to uniform element size of $h = (R_2 - R_1)/4 = 0.25$. In angle directions, this mesh contains four elements in $\tilde{\varphi}$ and μ directions, corresponding to inter-element values of $\tilde{\varphi} \in \{-\pi, -\pi/2, 0, \pi/2, \pi\}$ and $\mu \in \{-1, -0.5, 0, 0.5, 1\}$, respectively. For convergence analysis this mesh is uniformly refined in all directions by factors of 2. For example, for the next coarsest mesh $h = 0.125$ and 8 elements are used in each angle direction. Uniform space and angle polynomial orders of $p = 0$ to $p = 3$ are used for the analysis. The convergence rate of the discrete solution is obtained by determining the slope β_p of the logarithm of L2 norm of error $L_2(\varepsilon)$ versus the logarithm of the element size h. As shown in fig. 7, the asymptotic convergence rate of $\beta_p = p + 1$ is achieved for polynomial order p as $h \to 0$.

4.2 Verification of the DG method with the method of characteristics

A practical problem of radiation in an annular furnace with inner and outer radii of $R_1 = 1$ and $R_2 = 2$ is considered with inflow boundary conditions $I(R_1) = I(R_2) = 1$. There are no angular coupling integrals in (3) as $\kappa = 0$ and $\sigma_s = 0$. The extinction coefficient is $\beta = 0.01$. Since this problem does not have a closed-form exact solution, the method of characteristics is used to verify the DG solution.

For the method of characteristic, it is worth mentioning that a sparse zone exists along $\tilde{\varphi} = \pm\frac{1}{2}\pi$. While in this case 200 characteristic lines are used in each $r - \tilde{\varphi}$ plane, the solution points are still very sparse in the regions shown in fig. 8. To better show this sparsity and noting the symmetry of the solution with respect to $\tilde{\varphi} = 0$ plane, the solution I is only shown on the top half of the domain. As done for the next results, one can simply increase the number of characteristics lines to reduce the sparsity. However, for comparison of the two methods, it is noted that the DG method does not have this issue, since the solution is interpolated by polynomials over the entire space-angle domain.

The results for both methods are shown in fig. 9 in sliced $r - \tilde{\varphi}$ planes for $\mu = -0.5,\ 0,\ 0.5$. These planes are chosen since characteristic lines stay in them. For the method of characteristics, $\Delta l = 0.01$ and 2000 characteristic lines are used in each $r - z$ plane to generate the plots; *cf.* §2.2 and §3.2. As shown in fig. 9(a), there are two lines of strong discontinuity in I that coincide for all values of μ. The distance between these lines decreases and the discontinuity jump increases as r increases toward $R_2 = 2$. The cause of the change of the curvature of the discontinuity line and the form and width of high gradient solution features along r is the appearance of r in the

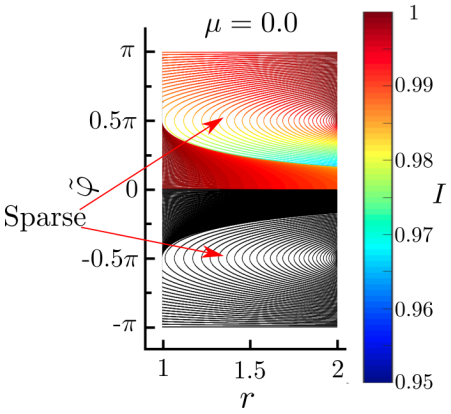

Figure 8: The results of the method of characteristic in a $r - \tilde{\varphi}$ plane, where $\tilde{\varphi} < 0$ shows the characteristics in black and $\tilde{\varphi} \geq 0$ shows the characteristics with the intensity field. The red arrows point to regions where characteristic lines are sparse.

denomonator of the equation for $\mathrm{d}\tilde{\varphi}$ in (9). As shown in fig. 9(b), the DG method is capable to accurately capture this discontinuity without much numerical oscillations around these lines with a moderately refined mesh of $32 \times 32 \times 32$ elements and $p = 3$. It is emphasized that one main advantage of DG methods over continuous finite element methods is their superior performance for problems with jumps and high gradient solutions features. Due to the structure of characteristic lines, such jumps in the solution are common for the axisymmetric RTE. This example demonstrates the advantage of using a DG method for this RTE formulation.

To compare the results of the DG method and the method of characteristics, a convergence study is performed in terms of the L2 error norm between the two solutions. That is, the high resolution solution of the method of characteristics plays the role of exact solution I^{M} in (22). The convergence rate of $\beta_p \approx 0.4$ is not improved by increasing the polynomial order. The limit in the convergence rate of the solution is due to the strong discontinuity lines that pass through finite elements. While the resolution improves, the transition region along the discontinuity lines which is proportional to the element size becomes narrower.

4.3 Benchmark problems between two concentric cylinders

4.3.1 Blackbody emission

The problem of a gray gas at radiative equilibrium between two concentric cylinders with infinite height is conducted and compared with the numerical results by Loyalka [40] which are accurate enough to be considered as the benchmark solution [2]. The ratio of inner and outer radii of the walls takes the values $R_1/R_2 = 0.1,\ 0.5,\ 0.9$. Moreover, the optical thickness, $\tau = \int_0^r \beta(r)\mathrm{d}r$, also changes in different cases by changing the extinction coefficient β. The inner surface is hot ($T_1 = 2000K$) and highly reflective ($\epsilon_1 = 0.1$); the outer surface is relatively cool ($T_2 = 400K$) and is a strong absorber ($\epsilon_2 = 0.9$). Inside the concentric cylinder, the medium is gray and non-scattering ($\sigma_s = 0$).

The nondimensional radiative heat transfer, Ψ, is defined as [40],

$$\Psi = \frac{q(\tau_1)}{J_1 - J_2}, \tag{23}$$

where $q(\tau_1)$ is the radiative flux density at $r = R_1$ ($\tau = \tau_1$). The radiative flux density at radius r is obtained by the inner product of the surface normal $\boldsymbol{n}_x$ and heat flux vector $\boldsymbol{q}(r)$,

$$q(r) = \boldsymbol{q}(r) \cdot \boldsymbol{n}_x, \qquad \text{where} \qquad \boldsymbol{q}(r) = \oint_{4\pi} I(\boldsymbol{r}, \hat{\boldsymbol{s}})\hat{\boldsymbol{s}}\mathrm{d}s'. \tag{24}$$

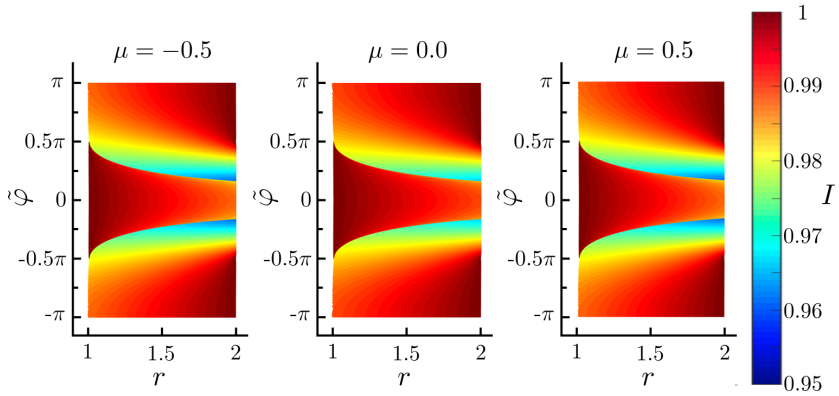

(a) Method of characteristics

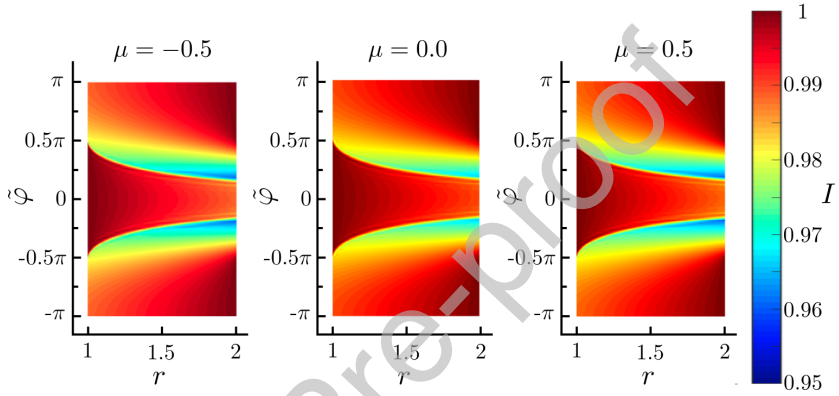

(b) DG method

Figure 9: Contour plots of radiation intensity for the problem in §4.2 for two different solution methods.

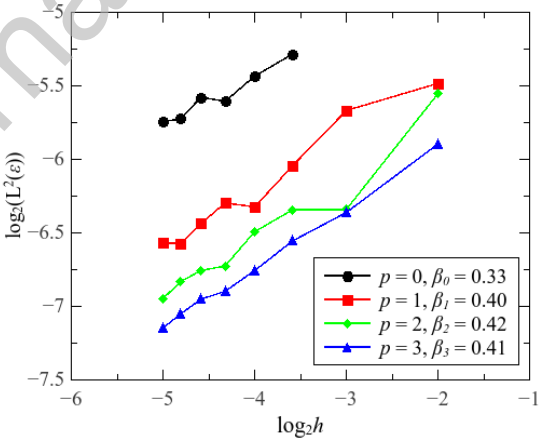

Figure 10: Convergence study of the DG RTE solution with respect to a high resolution reference solution obtained by the method of characteristics.

Since only inner surface is concerned, the surface normal $\boldsymbol{n}_x = (-1, 0, 0)$ is used for $r = R_1$ in $(e_r, e_{\varphi_x}, e_z)$ coordinate system; *cf.* fig. 1.

The values J_1 and J_2 are the radiosity of the walls at radii R_1 and R_2, respectively. They

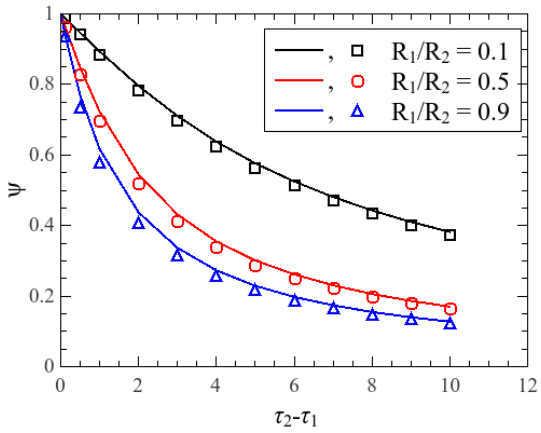

Figure 11: Nondimensional radiative heat transfer, Ψ, between concentric cylinders at radiative equilibrium against the optical thickness, $\tau_2 - \tau_1$, at different radius ratio, R_2/R_1. The solid lines are the numerical solution presented by Loyalka [40]; the hollow shapes (squares, circles and triangles) are the solutions by the DG method.

account for non-black emission and diffuse reflection. For wall $w \in \{1, 2\}$, J_w has the relation with net radiative flux $q_w = q(R_w)$ [40],

$$q_w = \frac{\epsilon_w}{1 - \epsilon_w}(\pi I_{bw} - J_w), \tag{25}$$

where the black-body radiation at wall w, denoted by I_{bw}, is obtained from (2). Since q_w and I_{bw} are computed from the solution to RTE and ϵ_w is the emissivity of wall w, J_w can be obtained from (25). Once J_1 and J_2 are obtained, Ψ is computed from (23).

A $16 \times 16 \times 16$ grid with polynomial order $p = 1$ is used for DG solutions. As shown in fig. 11, the DG results agree well with the numerical results by Loyalka [40]. It is observed that the nondimensional radiative heat transfer decreases with the increase of the optical thickness as well as the increase of the radius ratio. The effect of the radius ratio can be contributed to the fact that as $R_1/R_2 \to 0$ less energy is reflected from the inner boundary and most of the energy exits from the outer boundary. It is noticed that the difference between DG and reference solution is slightly larger for thinner optical thicknesses and the difference has overall lower values for smaller R_1/R_2 ratios. This may be contributed to numerical integration errors and other approximations involved in the solution method employed in [40].

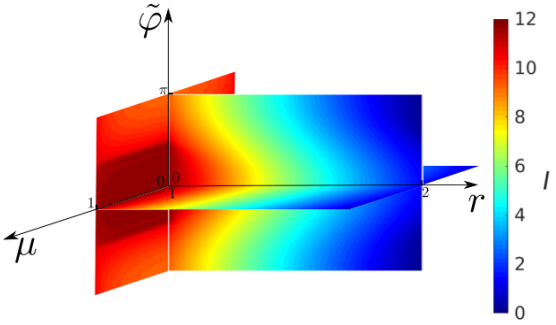

Figure 12: Contour plot of radiation intensity of the benchmark problem for $R_1/R_2 = 0.5$ and $\tau_2 - \tau_1 = 10$.

Comparing to the previous example in fig. 9(b), where strong discontinuity is inside the domain along the characteristic lines $r\sin\tilde{\varphi} = \pm 1$, the results with diffuse reflection on boundaries and emission in the domain seem much smoother; this is shown in fig. 12 for a particular case of $R_1/R_2 = 0.5$ and $\tau_2 - \tau_1 = 10$. In general, the angle integrations through scattering and black-body radiation terms, as well as emissive and diffusive terms on the boundary of domain in (5), smoothen the solution around the characteristic jump lines in fig. 9(b). These angle integral terms improve the accuracy and order of convergence of the DG method.

4.3.2 Anisotropic scattering

In this case, the enclosure of two infinite concentric cylinders with radii of $R_1 = 1$ and $R_2 = 2$ contains an anisotropic scattering medium with the cold inner wall with $I(R_1) = 0$ and isotropic incidence on outer wall with $I(R_2) = 1$. The extinction, absorption, and scattering coefficients are $\beta = 0.1$, $\kappa = 0$, and $\sigma_s = 0.05$, respectively. The Rayleigh scattering is used, where phase function $\Phi(\mu, \tilde{\varphi}, \mu', \tilde{\varphi}')$ is given,

$$\Phi(\mu, \tilde{\varphi}, \mu', \tilde{\varphi}') = \frac{3}{4}\left\{1 + \left[\sqrt{(1-\mu^2)(1-\mu'^2)}\cos(\tilde{\varphi} - \tilde{\varphi}') + \mu\mu'\right]^2\right\}. \tag{26}$$

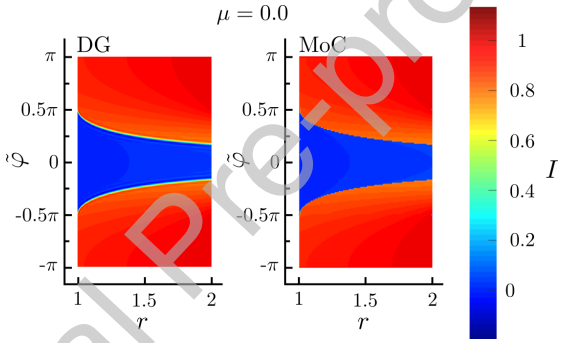

(a) Solutions with anisotropic scattering.

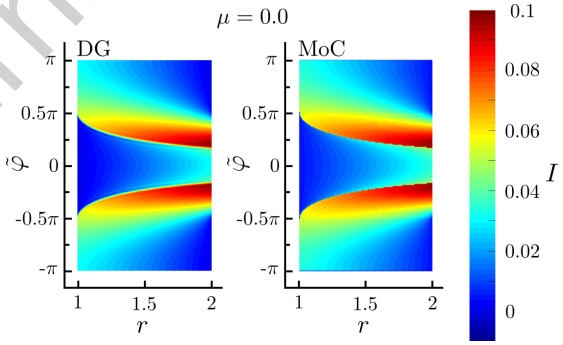

(b) Difference between the scattering solutions and the non-scattering solutions.

Figure 13: Contour plots of radiation intensity for the problem in §4.3.2 for $\mu = 0$ for two different methods. The left and right figures correspond to the solutions by the DG method and the method of characteristics (MoC), respectively.

A $64 \times 64 \times 64$ grid with polynomial order $p = 2$ is used for DG solutions. In the meanwhile, a $201 \times 201 \times 201$ structured grid with $\Delta l = 0.01$ is used for the backward iterative scheme of the method of characteristics; *cf.* §3.2.2. It took the iterative scheme 221 steps to converge with

a relative error of 1×10^{-12}. For the solutions presented here, the solution cost of the method of characteristics is about three times of that of the DG method. However, it is noted that due to several differences in the programming practices and languages of the two implementation and the limited set of comparisons of the two methods, this cost comparison is not expected to be thorough and conclusive. The results for both methods, as shown in fig. 13(a), indicate a strong discontinuity which is similar to the results in §4.2. Again, the DG method accurately captures the discontinuity without much numerical oscillations along the jumps, with coarser grid compared to the method of characteristics. It is noted that this problem was also solved with coarser resolutions by the DG method. The transition region where the discontinuity in the solution is represented by a rapid solution change in general is proportional to the element size; that is, as the element size tends to zero, the discontinuity is more accurately captured. Figure 13(b) shows the results of the difference between the solutions with anisotropic scattering and the solutions without scattering ,*i.e.,* $\sigma_s = 0$ for the two methods. It provides a better perspective of how the medium scatters the radiation energy. As shown, strong scattering is observed near the outflow outer boundary where rays intersect with the outer wall. Moreover, the backward scattering is weaker from the outer wall towards the inner wall.

5 Discussion and conclusions

A discontinuous Galerkin method for the solution of steady state radiative heat transfer between concentric cylinders, described by the one-dimensional RTE in cylindrical coordinates, was presented. The application of the discontinuous Galerkin method is described for problems in which radiation intensity varies over one dimension in space and two dimensions in angles. In this application, the RTE is spontaneously discretized over the space and angle by the DG method.

To discretize the angular directions, the spatial elements are extruded in two angular directions. This allows the basis function to be high order not only in space but also in angle. This aspect improves the convergence rate as shown in §4.1.2 and [38], compared to the hybrid methods that are capable of changing the order of accuracy only in space, such as hybrid (S_N) FEM [17, 18, 19, 20], (S_N) DG method [23, 24, 25, 26, 27, 28], and other hybrid methods [33, 34, 59, 60] which use a piece-wise constant or a delta function in angle. Specific to this RTE formulation, the discretization of the $\mathrm{d}I/\mathrm{d}\tilde{\varphi}$ term in (3) with finite difference in discrete ordinate method poses new implementation challenges and introduces additional discretization errors. For the DG formulation, the RTE is fully discretized in space and angle, so no additional scheme is needed to model this derivative term.

The use of DG formulation has several advantages. First, similar to continuous FEMs complex spatial geometries can be modeled with arbitrarily high order of accuracy in space. Second, inter-element continuity constraint is enforced weakly using the target flux I^*. In contrast, for the RTE formulation presented herein, a continuous space-angle FEM formulation would enforce a continuity constraint along the μ direction. This continuity condition is nonphysical when there are no angle-integration terms in (1) and (5). Moreover, the use of upstream values for I^* results in very accurate representation of solution, consistent with the characteristic structure of problem; as discussed DG methods have a superior performance to continuous FEMs in capturing jumps in solution, such as those observed in $r - \tilde{\varphi}$ planes in fig. 9. Third, as discussed in detail in [38], while both DG in angle and spherical harmonic method can achieve arbitrary high order of accuracy in angle, the former has a better performance for problems with concentrated point or line sources.

Several numerical examples were presented for this DG formulation. The convergence study was conducted for both smooth and discontinuous solutions. While for the latter, the convergence rate is relatively poor as shown in fig. 10, the space-angle DG method is still able to accurately capture discontinuities in the solution in $r - \tilde{\varphi}$ planes. Moreover, the benchmark

problem from [40] shows the high accuracy of the DG method for different optical thicknesses and ratios of the inner to outer radii. The last problem shows that the DG has a good flexibility for solving the RTE with complex properties, *e.g.,* scattering in an anisotropic medium.

To verify the results by the DG solver, the method of characteristic is employed for the one-dimensional cylindrical RTE. The method of characteristic performs better, especially, with respect to the strong discontinuity, since the intensity is calculated along the corresponding characteristics without the jumps involved for individual line solutions. However, the difficulty in modeling complex geometries (boundary condition particularly) and the low iteration convergence rate when angular integration terms are involved are its disadvantages. The transition region at the discontinuity, for example in fig. 13, is inevitable for the DG and other finite element / volume methods when the discontinuity passes through the finite elements / volumes. Still, DG methods generally outperform other mesh-based methods. For example, as demonstrated in [15] continuous FEMs can suffer even worse numerical oscillations around discontinuities. We have discussed these advantages of the DG method for a planar-parallel RTE formulation [38] using a problem with a concentrated source term.

As an extension to this work, it is noted that the discontinuity can be exactly *tracked* with DG methods if it can be aligned with the element boundaries. Moreover, adaptive schemes can accurately and efficiently *capture* such discontinuities in narrower bands. Finally, DG methods are very flexible to change the element order (p-enrichment) or size (h-adaptive), without the need of transition elements used in adaptive continuous FEMs. We plan to extend the novel adaptive operations proposed in [61] from space and spacetime to the space-angle RTE problem. Another important extension to this work is the formulation of an iterative solution of the RTE when angular integration terms are present. In this case, the system stiffness matrix is very dense and even for moderate resolutions of the grid in space and angle, this matrix may not fit in computer RAM memory. We are currently working on an iterative scheme that each time only one slab of the domain in $r - \tilde{\varphi}$ plane is solved. This would enable solving the problem in §4.3.2 with much higher resolutions.

References

[1] R. Siegel, J. Howell, Thermal Radiation Heat Transfer, 4th Edition, Taylor and Francis, 2002.

[2] M. F. Modest, Radiative heat transfer, Academic press, 2013.

[3] P. J. Coelho, Advances in the discrete ordinates and finite volume methods for the solution of radiative heat transfer problems in participating media, Journal of Quantitative spectroscopy and Radiative transfer 145 (2014) 121–146.

[4] J. Reddy, V. Murty, Finite-element solution of integral equations arising in radiative heat transfer and laminar boundary-layer theory, Numerical Heat Transfer, Part B: Fundamentals 1 (3) (1978) 389–401.

[5] W. Fiveland, Discrete-ordinates solutions of the radiative transport equation for rectangular enclosures, Journal of heat transfer 106 (4) (1984) 699–706.

[6] S. T. Thynell, Discrete-ordinates method in radiative heat transfer, International journal of engineering science 36 (12-14) (1998) 1651–1675.

[7] K. F. Evans, The spherical harmonics discrete ordinate method for three-dimensional atmospheric radiative transfer, Journal of the Atmospheric Sciences 55 (3) (1998) 429–446.

[8] M. F. Modest, J. Cai, W. Ge, E. Lee, Elliptic formulation of the simplified spherical harmonics method in radiative heat transfer, International Journal of Heat and Mass Transfer 76 (2014) 459–466.

[9] M. Benassi, R. Garcia, A. Karp, C. Siewert, A high-order spherical harmonics solution to the standard problem in radiative transfer, The Astrophysical Journal 280 (1984) 853–864.

[10] L. Briggs, W. Miller Jr, E. Lewis, Ray-effect mitigation in discrete ordinate-like angular finite element approximations in neutron transport, Nuclear Science and Engineering 57 (3) (1975) 205–217.

[11] J. C. Chai, H. S. Lee, S. V. Patankar, Ray effect and false scattering in the discrete ordinates method, Numerical Heat Transfer, Part B Fundamentals 24 (4) (1993) 373–389.

[12] S. Rukolaine, M. Vasilyev, V. Yuferev, A. Galyukov, Numerical solution of axisymmetric radiative transfer problems in arbitrary domains using the characteristic method, Journal of Quantitative Spectroscopy and Radiative Transfer 73 (2-5) (2002) 205–217. doi:10.1016/S0022-4073(01)00204-7.
URL https://linkinghub.elsevier.com/retrieve/pii/S0022407301002047

[13] M. B. Salah, F. Askri, K. Slimi, S. B. Nasrallah, Numerical resolution of the radiative transfer equation in a cylindrical enclosure with the finite-volume method, International Journal of Heat and Mass Transfer 47 (10-11) (2004) 2501–2509.

[14] E. E. Lewis, W. F. Miller, Computational methods of neutron transport, John Wiley and Sons, Inc, United States, 1984.

[15] J. J. Duderstadt, W. R. Martin, Transport theory., John Wiley & Sons, New York, United States, 1979.

[16] S. Chandrasekhar, Radiative transfer, Courier Corporation, 2013.

[17] Y. Shmyglevskii, Calculation of radiative transfer by Galerkin's method, USSR Computational Mathematics and Mathematical Physics 13 (2) (1973) 157 – 168. doi:http://dx.doi.org/10.1016/0041-5553(73)90138-9.
URL http://www.sciencedirect.com/science/article/pii/0041555373901389

[18] M. S. Abdel Krim, M. T. Attia, M. A. Madkour, Application of the superconvergence properties of the Galerkin approximation to radiative transfer, Astrophysics and Space Science 186 (1) (1991) 89–99. doi:10.1007/BF00644622.
URL https://doi.org/10.1007/BF00644622

[19] M. Razzaghi, S. Oppenheimer, F. Ahmad, Numerical solution of radiative transfer problems in a slab medium by Galerkin-type approximation techniques, Physica Scripta 64 (2) (2001) 97.
URL http://stacks.iop.org/1402-4896/64/i=2/a=001

[20] M. Sallah, M. T. Attia, On Galerkin technique for transient radiative heat transfer in finite thin media, Numerical Heat Transfer, Part B: Fundamentals 56 (4) (2009) 323–334. arXiv:http://dx.doi.org/10.1080/10407790903126682, doi:10.1080/10407790903126682.
URL http://dx.doi.org/10.1080/10407790903126682

[21] H. Egger, M. Schlottbom, A class of Galerkin schemes for time-dependent radiative transfer, SIAM Journal on Numerical Analysis 54 (6) (2016) 3577–3599. arXiv:https://doi.org/10.1137/15M1051336, doi:10.1137/15M1051336.
URL https://doi.org/10.1137/15M1051336

[22] T. Reed, William H and Hill, Triangular mesh methods for the neutron transport equation, Tech. Rep. LA-UR-73-479; CONF-730414-2, Los Alamos Scientific Lab., N.Mex. (USA), Ann Arbor, Michigan, USA (1973).

[23] L. H. Liu, L. J. Liu, Discontinuous finite element method for radiative heat transfer in semitransparent graded index medium, Journal of Quantitative Spectroscopy and Radiative Transfer 105 (3) (2007) 377–387. doi:10.1016/j.jqsrt.2006.11.017.

[24] J. Zhao, L. Liu, Discontinuous spectral element method for solving radiative heat transfer in multidimensional semitransparent media, Journal of Quantitative Spectroscopy and Radiative Transfer 107 (1) (2007) 1–16.

[25] W. Han, J. Huang, J. A. Eichholz, Discrete-ordinate discontinuous Galerkin methods for solving the radiative transfer equation, SIAM Journal on Scientific Computing 32 (2) (2010) 477–497. arXiv:https://doi.org/10.1137/090767340, doi:10.1137/090767340.
URL https://doi.org/10.1137/090767340

[26] J. EIchholz, Discontinuous Galerkin methods for the radiative transfer equation and its approximations, Dissertation, University of Iowa (2011).
URL http://ir.uiowa.edu/cgi/viewcontent.cgi?article=2519&context=etd

[27] M. M. Crockatt, A. J. Christlieb, C. K. Garrett, C. D. Hauck, An arbitrary-order, fully implicit, hybrid kinetic solver for linear radiative transport using integral deferred correction, Journal of Computational Physics 346 (2017) 212 – 241.

[28] D. Yuan, J. Cheng, C.-W. Shu, High order positivity-preserving discontinuous Galerkin methods for radiative transfer equations, SIAM Journal on Scientific Computing 38 (5) (2016) A2987–A3019. arXiv:https://doi.org/10.1137/16M1061072, doi:10.1137/16M1061072.
URL https://doi.org/10.1137/16M1061072

[29] V. M. Laboure, R. G. McClarren, C. D. Hauck, Implicit filtered P_N for high-energy density thermal radiation transport using discontinuous Galerkin finite elements, Journal of Computational Physics 321 (2016) 624 – 643.

[30] L. Liu, Finite element solution of radiative transfer across a slab with variable spatial refractive index, International Journal of Heat and Mass Transfer 48 (11) (2005) 2260–2265. doi:10.1016/j.ijheatmasstransfer.2004.12.045.
URL https://linkinghub.elsevier.com/retrieve/pii/S0017931005000967

[31] J. Pontaza, J. Reddy, Least-squares finite element formulations for one-dimensional radiative transfer, Journal of Quantitative Spectroscopy and Radiative Transfer 95 (3) (2005) 387–406.

[32] R. O. Castro, J. P. Trelles, Spatial and angular finite element method for radiative transfer in participating media, Journal of Quantitative Spectroscopy and Radiative Transfer 157 (2015) 81–105. doi:10.1016/j.jqsrt.2015.02.008.
URL http://dx.doi.org/10.1016/j.jqsrt.2015.02.008

[33] H. Gao, H. Zhao, A fast-forward solver of radiative transfer equation, Transport Theory and Statistical Physics 38 (3) (2009) 149–192. arXiv:http://dx.doi.org/10.1080/00411450903187722, doi:10.1080/00411450903187722.
URL http://dx.doi.org/10.1080/00411450903187722

[34] H. Gao, H. Zhao, Analysis of a numerical solver for radiative transport equation, Mathematics of Computation 82 (5) (2013) 153–172. arXiv:https://doi.org/10.1090/S0025-5718-2012-02605-6, doi:10.1090/S0025-5718-2012-02605-6.
URL https://doi.org/10.1090/S0025-5718-2012-02605-6

[35] J. Kophazi, D. Lathouwers, A space angle DGFEM approach for the boltzmann radiation transport equation with local angular refinement, Journal of Computational Physics 297 (2015) 637 – 668. doi:http://dx.doi.org/10.1016/j.jcp.2015.05.031.
URL http://www.sciencedirect.com/science/article/pii/S0021999115003654

[36] D. Kitzmann, J. Bolte, A. B. C. Patzer, Discontinuous Galerkin finite element methods for radiative transfer in spherical symmetry, A&A 595 (2016) A90. doi:10.1051/0004-6361/201628578.
URL https://doi.org/10.1051/0004-6361/201628578

[37] P. L. Clarke, H. Wang, J. M. Garrard, R. Abedi, S. Mudaliar, A discontinuous Galerkin method for the solution of one dimensional radiative transfer equation, in: 2018 USNC-URSI Radio Science Meeting (Joint with AP-S Symposium), Boston, Massachusetts, USA, July 8-13, 2018, pp. 71–72.

[38] P. Clarke, H. Wang, J. Garrard, R. Abedi, S. Mudaliar, Space-angle discontinuous Galerkin method for plane-parallel radiative transfer equation, Journal of Quantitative Spectroscopy and Radiative Transfer 233 (2019) 87–98.

[39] J. R. Howell, M. Perlmutter, Radiant transfer through a gray gas between concentric cylinders using Monte Carlo, ASME Journal of Heat Transfer 86 (2) (1964) 169–179. doi:10.1115/1.3687090.

[40] S. K. Loyalka, Radiative heat transfer between parallel plates and concentric cylinders, International Journal of Heat and Mass Transfer 12 (11) (1969) 1513–1517. doi:10.1016/0017-9310(69)90030-1.

[41] A. S. Kesten, Radiant heat flux distribution in a cylindrically-symmetric nonisothermal gas with temperature-dependent absorption coefficient, in: Radiative Energy Transfer, Elsevier, 1968, pp. 419–434.

[42] D. Pandey, A. Cogley, An integral solution procedure for radiative transfer in concentric cylindrical media, American Society of Mechanical Engineers (1983).

[43] R. Viskanta, M. Mengüç, Radiation heat transfer in combustion systems, Progress in Energy and Combustion Science 13 (2) (1987) 97–160.

[44] D. A. Blank, S. C. Mishra, Use of the 2-d collapsed dimension method in absorbing-emitting media with isotropic scattering, in: Radiative Transfer I. Proceedings of the First International Symposium on Radiation Transfer, Begel House Inc., 1995.

[45] J. R. Howell, M. P. Menguc, R. Siegel, Thermal radiation heat transfer, CRC press, 2010.

[46] K. C. Tang, M. Q. Brewster, K-distribution analysis of gas radiation with nongray, emitting, absorbing, and anisotropic scattering particles, Journal of Heat Transfer 116 (4) (1994) 980–985.

[47] R. Goody, R. West, L. Chen, D. Crisp, The correlated-k method for radiation calculations in nonhomogeneous atmospheres, Journal of Quantitative Spectroscopy and Radiative Transfer 42 (6) (1989) 539–550.

[48] F. Liu, G. J. Smallwood, Ö. L. Gülder, Application of the statistical narrow-band correlated-k method to low-resolution spectral intensity and radiative heat transfer calculations - effects of the quadrature scheme, International Journal of Heat and Mass Transfer 43 (17) (2000) 3119–3135.

[49] M. J. Yu, S. W. Baek, J. H. Park, An extension of the weighted sum of gray gases non-gray gas radiation model to a two phase mixture of non-gray gas with particles, International Journal of Heat and Mass Transfer 43 (10) (2000) 1699–1713.

[50] V. P. Solovjov, B. W. Webb, Multilayer modeling of radiative transfer by slw and cw methods in non-isothermal gaseous medium, Journal of Quantitative Spectroscopy and Radiative Transfer 109 (2) (2008) 245–257.

[51] C. Cannon, Line transfer in two dimensions, The Astrophysical Journal 161 (1970) 255.

[52] R. Abedi, R. B. Haber, B. Petracovici, A spacetime discontinuous Galerkin method for elastodynamics with element-level balance of linear momentum, Computer Methods in Applied Mechanics and Engineering 195 (2006) 3247–73.

[53] R. K. Pal, R. Abedi, A. Madhukar, R. B. Haber, Adaptive spacetime discontinuous Galerkin method for hyperbolic advection-diffusion with a non-negativity constraint, International Journal for Numerical Methods in Engineering 105 (13) (2016) 963–89.

[54] R. Abedi, S. Mudaliar, An asynchronous spacetime discontinuous Galerkin finite element method for time domain electromagnetics, Journal of Computational Physics 351 (Supplement C) (2017) 121–144. doi:https://doi.org/10.1016/j.jcp.2017.09.001.
URL http://www.sciencedirect.com/science/article/pii/S0021999117306514

[55] Q. Zhan, Q. Ren, M. Zhuang, Q. Sun, Q. H. Liu, An exact riemann solver for wave propagation in arbitrary anisotropic elastic media with fluid coupling, Computer Methods in Applied Mechanics and Engineering 329 (2018) 24–39.

[56] R. Abedi, R. B. Haber, Riemann solutions and spacetime discontinuous Galerkin method for linear elastodynamic contact, Computer Methods in Applied Mechanics and Engineering 270 (2014) 150–77.

[57] Q. Zhan, M. Zhuang, Y. Mao, Q. H. Liu, Unified riemann solution for multi-physics coupling: Anisotropic poroelastic/elastic/fluid interfaces, Journal of Computational Physics (2019) 108961.

[58] R. Abedi, R. B. Haber, Spacetime simulation of dynamic fracture with crack closure and frictional sliding, Advanced Modeling and Simulation in Engineering Sciences 5 (1) (2018) 22, Equal contribution authorship.

[59] X. Cui, B. Q. Li, A discontinuous finite-element formulation for internal radiation problems, Numerical Heat Transfer, Part B: Fundamentals 46 (3) (2004) 223–242. doi:10.1080/10407790490475274.

[60] X. Cui, B. Q. Li, Discontinuous finite element solution of 2-d radiative transfer with and without axisymmetry, Journal of Quantitative Spectroscopy and Radiative Transfer 96 (3-4) (2005) 383–407. doi:10.1016/j.jqsrt.2004.11.007.

[61] R. Abedi, R. B. Haber, S. Thite, J. Erickson, An h–adaptive spacetime–discontinuous Galerkin method for linearized elastodynamics, Revue Européenne de Mécanique Numérique (European Journal of Computational Mechanics) 15 (6) (2006) 619–42.

H. Wang carried out the numerical calculations

R. Abedi and S. Mudaliar conceived and formulated the problem

Declaration of interests

☒ The authors declare that they have no known competing financial interests or personal relationships that could have appeared to influence the work reported in this paper.

☐The authors declare the following financial interests/personal relationships which may be considered as potential competing interests: